



# Evaluation of the sub-annual sea level anomalies in the continental shelf of the Southwestern Atlantic and their relation to wind variability

Marie-Christin Juhl<sup>1</sup> · Marcello Passaro<sup>1</sup> · Denise Dettmering<sup>1</sup> · Martin Saraceno<sup>2,3,4</sup>

Received: 20 September 2023 / Accepted: 17 June 2024 / Published online: 1 July 2024  
© The Author(s) 2024

## Abstract

We have analyzed the relationship between wind variability and sea level anomalies (SLA) on the Southwestern Atlantic Continental Shelf, focusing on sub-annual temporal scales. For this, we tested the capability of gridded altimetry to represent wind-driven SLA and compared results using an oceanographic model and tide gauge data. The present study used coherence analysis to analyze frequencies for which SLA and wind stress are coherent. The altimetry-SLA were found to have less energy below the three-month period compared to the model SLA. The coherence of along-shore wind stress and altimetry SLA was only significant for > 50 days (d), while the model SLA showed significant agreement in all periods considered, 20 d to annual. We further showed that geostrophic velocities on the continental shelf agreed significantly with SLA for > 50 d. As a result of an Empirical Orthogonal Function (EOF) analysis, we found that the second mode is highly coherent with the along-shore wind stress and accounts for 18.1% and 10.7% of variability in the model and altimetry sea level anomalies, respectively.

**Keywords** Satellite altimetry · Gridded sea level anomalies · Southwestern Atlantic Continental Shelf

## 1 Introduction and background

Continental shelf regions serve as transition and buffer zones between land and open ocean, making their comprehension critical for oceanic observations. The provision of sea surface height from radar altimetry has dramatically improved our

knowledge of oceanic processes, thanks to 30 years of globally distributed data (International Altimetry Team 2021). Nevertheless, the comprehension of the oceanic processes that affect sea level anomalies (SLA) is particularly challenging in the coastal and continental shelf regions (Volkov et al. 2007). Here, waves, tidal currents, energy fluxes, and river discharges occur on short spatial and temporal scales (Woodworth et al. 2019). These shelf processes also affect the coastal regions, thus further determining, e.g., sea level extremes, primary production, carbon fluxes, and sediment transport (Simpson and Sharples 2012; Berden et al. 2022).

The Southwestern Atlantic Continental Shelf is recognized as one of the hot spots of marine biodiversity in the world ocean (Ramirez et al. 2017) and a significant sink of atmospheric CO<sub>2</sub> (Kahl et al. 2017). Research on Southwestern Atlantic Continental Shelf dynamics has often focused on the Rio de la Plata estuary and the surrounding shelf (e.g., Saraceno et al. 2014; Meccia et al. 2009; Combes and Matano 2018), being influenced by substantial freshwater input from river discharge. In particular, several studies have demonstrated the importance of wind as a driver of sea

Responsible Editor: Emma Young

✉ Marie-Christin Juhl  
mariechristin.juhl@tum.de

<sup>1</sup> Deutsches Geodätisches Forschungsinstitut der Technischen Universität München, Arcisstrasse 21, 80333 München, Germany

<sup>2</sup> Centro de Investigaciones del Mar y la Atmosfera (CIMA/CONICET-UBA), Buenos Aires, Argentina

<sup>3</sup> Departamento de Ciencias de la Atmósfera y los Océanos, Facultad de Ciencias Exactas y Naturales, Universidad de Buenos Aires (DCAO, FCEN-UBA), Buenos Aires, Argentina

<sup>4</sup> Instituto Franco-Argentino para el Estudio del Clima y sus Impactos (IRL 3351 IFAECI/CNRS-IRD-CONICET-UBA), Buenos Aires, Argentina

level variability from low frequencies to seasonal scales: On inter-annual scales, Combes and Matano (2019) connected perturbations in the Pacific with inter-annual SLA on the Patagonian Continental Shelf, while several other studies also connected the sea level variations to ENSO (Saraceno et al. 2014) or the Southern Annular Mode (Lago et al. 2021). Evidence for wind as a driver of SLA on the continental Shelf was shown by several previous studies with a focus on low-frequency variations (Bodnariuk et al. 2021; Raicich 2008). From annual to sub-annual periods in the region, Strub et al. (2015) showed a correlation between altimetry-based SSH and wind at a monthly resolution, revealing that seasonal changes are mainly wind-driven north of the Rio de la Plata. Moreover, using a unique array of in situ measurements of currents, bottom pressure, and a coastal tide gauge, Lago et al. (2021) showed that sea surface height variability is driven by the cross-shore pressure gradients generated by the alongshore wind stress at all frequencies. Ruiz Etcheverry et al. (2016) have already demonstrated that annual changes in SLA south of 36°S are primarily due to steric effects. Instead, our study focuses on understanding the contribution of wind variability. Our aim in this work is to analyze the relationship between wind variability and the SLA on the wider continental shelf, with a particular focus on sub-annual temporal scales. In our analysis, we also consider the annual signal to better interpret our results compared to the previous literature. Additionally, Saraceno et al. (2014) have shown that significant SLA variability exists in our area of interest (27–40°S) across all timescales resolved by altimeter data (>20 d), while Lago et al. (2021) and Ferrari et al. (2017) demonstrated that multi-satellite gridded altimetry data compared better with in-situ data than along-track data in the study region.

The lack of tide gauge stations with continuous, long-term sea level data limits our knowledge of coastal SLA and their drivers at the Southwestern Atlantic Continental Shelf compared to other continental shelves. Several previous studies obtained knowledge about continental shelf dynamics using numerical simulations (Combes and Matano 2018; Meccia et al. 2009; Palma et al. 2004).

In this study, we primarily utilize gridded altimetry data and compare them with data from tide gauges and a numerical model. We focus on coherence analysis, instead of correlation only, with the aim of better identifying the role of wind in determining sea level variations at different frequencies as in, e.g., Dong et al. (2006), Ryan and Noble (2006) and Stramska (2013). Using coherence analysis allows us to obtain a thorough assessment of agreement between two time series across different frequencies. Furthermore, we employ Empirical Orthogonal Function (EOF) analysis of SLA to decompose the SLA data and analyze modes of variability connected to wind forcing.

## 2 Data and methods

### 2.1 Data

#### 2.1.1 SLA and geostrophic velocity

The gridded SLA data for this analysis were obtained from the Copernicus Marine Environment Service (CMEMS) based on global gridded SSH at a daily resolution (product identifier: SEALEVEL\_GLO\_PHY\_L4\_MY\_008\_047). The product includes data from multiple satellite missions, which were cross-calibrated and corrected for atmospheric and instrumental errors. The data originate from pre-processed level L3 along-track data and are gridded and interpolated on a 0.25°x0.25° global grid. Ballarotta et al. (2019) give an estimate of the product's effective resolution to be 14–21 d temporally and 150–250 km spatially within the study region. Along-track data on level L3 are processed concerning instrumental and atmospheric corrections. The SLA are corrected for tides using the FES2014 tide model. Geostrophic velocity components are computed similarly to the model geostrophic velocities for consistency (see Section 2.2.2).

#### 2.1.2 DAC

The Dynamic Atmosphere Correction (DAC) corrects for inverse barometer effect as well as for the dynamic atmospheric component of the sea level variability, including the high-frequency variability due to wind, which is poorly sampled by the altimetry constellation and would otherwise appear aliased over lower frequencies (Stammer et al. 2000). DAC data were obtained from Aviso<sup>1</sup> and interpolated on the SLA grid, as well as tide gauge location (used for validation, see Section 3.1).

#### 2.1.3 Tide gauge data

We obtained in-situ sea-level observations from tide gauge stations, with hourly sea-level data collected and distributed through the GESLA3 (Global Extreme Sea Level Analysis Version 3) framework (Haigh et al. 2023). The stations are listed with their available length in time in Table 1, and their location is marked on the map; see Section 2.3.

Daily averaging was applied to SLA data from tide gauge observations to make them comparable with daily altimeter-based SLA. No outliers were excluded because averaging already smooths the time series, thus damping possible out-

<sup>1</sup> Dynamic atmospheric Corrections are produced by CLS using the Mog2D model from Legos and distributed by Aviso+, with support from CNES (<https://www.aviso.altimetry.fr/>)

**Table 1** The correlation coefficient of daily SLA from tide gauges and altimetry ( $corr_{alt}$ ) and from tide gauge and model ( $corr_{mod}$ ) at tide gauge locations (Fig. 2) between 1993–2019

	site name	latitude	longitude	distance	available time period	length	$corr_{mod}$	$corr_{alt}$
1	Macaé	-22.23	-41.47	3.89	2001-07-13 - 2008-12-31	2415	0.81	0.39
2	Ilha Fiscal RJ	-22.90	-43.16	2.19	1993-01-01 - 2013-12-31	7669	0.76	0.32
3	Ubatuba	-23.50	-45.12	3.43	2013-06-03 - 2017-07-11	1437	0.90	0.44
4	Cananeia	-25.02	-47.92	9.43	2014-01-29 - 2016-10-29	5893	0.89	0.32
5	Imbituba	-28.23	-48.65	2.76	2001-08-22 - 2010-12-31	3131	0.89	0.49
6	Rio Grande	-32.14	-52.10	3.69	2001-06-01 - 2003-12-31	610	0.77	0.31
7	Mar del Plata	-38.03	-57.53	4.70	2004-11-15 - 2018-12-31	4659	0.91	0.36
8	Puerto Madryn	-42.76	-65.03	2.84	2010-03-14 - 2018-12-31	3190	0.93	0.18
9	Puerto Deseado	-47.75	-65.92	6.11	2010-03-17 - 2018-12-31	1766	0.55	0.20
10	Port Stanley	-51.75	-57.93	1.12	1993-01-01 - 2014-01-31	6960	0.57	0.39
11	Ushuaia	-54.80	-68.30	31.08	1996-01-01 - 2018-12-31	5787	0.84	0.15
12	Puerto Williams	-54.93	-67.62	2.82	1993-01-01 - 1998-12-31	1985	0.68	0.13

Stations are listed from North to South. The distance from the altimetry grid point to the station is given in km, and the length of time series within the available time period (excluding gaps) in days, respectively

liers. We obtained SLA from the sea level data by extracting the mean from each time series. Tide filtering is applied by using a 40h-Loess filter. SLA connected to DAC were removed for comparison with DAC-corrected SLA from altimetry in the validation.

### 2.1.4 Wind

Gridded wind data were obtained from CMEMS (product identifier: WIND\_GLO\_WIND\_L4\_REP\_OBSERVATIONS\_012\_006). Wind stress data from scatterometry of various missions were distributed, combined, and interpolated in daily resolution on a 0.25°x0.25° grid (consistent with altimetry SLA, see above). Wind stress data are split into eastward/northward components (equivalent to a wind vector), and in the present work, we extracted the along-shore component, preserving the grid resolution.

### 2.1.5 Model

For comparison, we used Sea Surface Height (SSH) from the numerical model run from CMEMS: (product ID: GLOBAL\_MULTIYEAR\_PHY\_001\_030, <https://doi.org/10.48670/moi-00021>) at a daily resolution. The model uses assimilation of along-track SLA observations from all altimetric missions and is thus not completely independent from gridded altimetry SLA. The original spatial resolution of 1/12° was scaled down to 1/4° to match the gridded altimetry product. SLA from the SSH were obtained by removing the mean over the full period from 1993 to 2019 per grid point. The model SLA have no inverse barometer effect included

and thus needs no correction. We computed the geostrophic currents from the model SLA (see Section 2.2) to make the model data comparable with the altimetry data.

## 2.2 Methods

### 2.2.1 Along-shore wind components

The wind data are given as the wind stress in Pa. The northward ( $w_{north}$ ) and eastward wind ( $w_{east}$ ) wind stress components were used to calculate the wind stress direction ( $\theta$ ) and decompose the wind stress data  $w$  with respect to topography into along-shore surface downward wind stress. Therefore, the continental coastline in the study area was treated as a line rotated by a constant angle (39°) to the geographic Meridian (see Section 2.3 for reference). We calculated the along-shore wind stress component by Eq. 1 and the actual wind angle  $\theta$  per grid cell and time step Eq. 2.

$$w_{along} = w \cdot \cos(\theta - 39^\circ) \tag{1}$$

$$\theta = \frac{180}{\pi} \cdot \arctan(w_{north}, w_{east}) \tag{2}$$

By convention, the along-shore wind is orientated northeastward for positive values.

### 2.2.2 Geostrophic velocities

From the SLA of the model and altimetry, we derived the geostrophic velocities by applying the geostrophic relation

using the following equations defined on latitudes  $j$  and longitudes  $i$ :

$$u_g = \frac{-g}{f(j)} \cdot \frac{\Delta SLA_{i,i-1}}{dist_{(i,i-1)}} \quad (3)$$

$$v_g = \frac{g}{f(j)} \cdot \frac{\Delta SLA_{j,j-1}}{dist_{(j,j-1)}} \quad (4)$$

with the acceleration of gravity  $g$ , the Coriolis parameter  $f$  at the latitude  $j$ , and the distance of two points in m  $dist$ . The along-shore component was computed similarly to the wind stress data above.

### 2.2.3 Coherence

Magnitude-squared coherence (referred to as coherence from now on) is used to express the similarity of two time series. Coherence provides a measure of the degree to which the variance of one variable is explained by the other. To compute coherence, each time series is transformed in the frequency domain using spectral analysis. Following (Thomson and Emery 2014), the auto-spectral density  $S_{xx}$  and the cross-spectral density  $S_{xy}$  of two signals  $x(t)$ ,  $y(t)$  can be obtained as the Fourier-transform of the auto-correlation  $R_{xx}$  as well as the cross-correlation function  $R_{xy}$  (of an arbitrary time lag  $\tau$ ) for the time series  $x(t)$ ,  $y(t)$ . Using the Fourier transform and the auto-correlation function of a signal  $x(t)$ , it is possible to compute the variance per unit frequency as:

$$S_{xx}(f) = \int_0^{\infty} R_{xx} e^{-i2\pi f \tau} d\tau \quad (5)$$

If we consider two time-dependent signals  $x(t)$  and  $y(t)$  and their cross-correlation  $R_{xy}$  (similar to Eq. 5), it is possible to compute the coherence  $C_{xy}(f)$  as:

$$C_{xy}(f) = \frac{|S_{xy}(f)|^2}{S_{xx}(f)S_{yy}(f)} \quad (6)$$

where  $S_{xy}(f)$  is the cross-spectral density between  $x(t)$  and  $y(t)$ , while  $S_{xx}(f)$ ,  $S_{yy}(f)$  are the auto-spectral densities. The cross-spectral density  $S_{xy}(f)$  is estimated as in Eq. 5 using cross-correlation from two individual signals  $x(t)$ ,  $y(t)$ . The cross-spectral density is a complex quantity that measures the correlation of the amplitudes as the real and the relative phase angle as its imaginary part. Further, the imaginary part holds the information on a possible phase lag of the two time series, valid in combination with a significant coherence. The application of the steps to the wind and SLA time series is illustrated in Fig. 1. The established practice is to apply a Hanning window before computing the coherence to avoid spectral leakage (Lyon 2009). In our case, we selected

a Hanning window with a length of 704 d. As a frequency-dependent measure, coherence allows for the independent assessment of agreement between two time series within specific frequency bands. This approach diverges from the conventional correlation analysis, which considers overall agreement regardless of frequency (see, e.g., Thomson and Emery (2014) for details). Based on the daily input data and the chosen window length of 704 d, the estimated coherence covered frequencies from 2 to 704 d. We selected the following frequency bands (expressed as the period in d) for interpretation of sub-annual process analysis: 20-30 d, 30-50 d, 50-79 d, 79-140 d, 140-234 d (covering semi-annual cycle) in addition to the annual period (at half the window length at 352 d). Note that periods of  $< 20$  d are below the effective altimetry resolution and therefore disregarded here.

The threshold for significant coherence  $c_{sig}$  at the 95% confidence level follows from the window length applied. One also has to consider the overlap of 50%, which nearly doubles the number of segments used for coherence estimation. Thus, a coherence above 0.32 can be considered significant at a 95%-confidence interval for 27 years (Jan. 1993- Dec. 2019).

### 2.2.4 EOF analysis

Empirical Orthogonal Functions (EOF) were used in the present study to decompose the SLA data in time and space by calculating the eigenvector and eigenvalues of the covariance matrix, as in Hendricks et al. (1996). The resulting principle components contain the temporal signal and spatial information belonging to several modes, often called "modes of variability," which are enumerated depending on their relative contribution (eigenvalues) to the variance in descending order. Thus, the first EOF mode describes the largest contribution to the total variance of the input signal. The decomposed time (principal components) and space (eigenvector) information of each EOF mode can be used to reconstruct the input variable from selected variability modes separately. The results of the EOF decomposition are highly dependent on the spatial and temporal coverage of the input data. In order to decouple the continental shelf processes affecting the sea level variability from the rest of the domain, we applied the EOF analysis to all data located on the continental shelf (above the 200 m isobath) within the study area (see Section 2.3), as similarly done in, e.g., Combes and Matano (2019).

### 2.3 Area of study

The present research focuses on the Southwestern Atlantic Continental Shelf from 20-55°S and 40-70°W (from now on referred to as the study area). The Southwestern Atlantic



**Fig. 1** Coherence at 55.75°W, 36.25°S. Time series of along-shore wind stress (a) and SLA (c). Auto-spectral density for a given time series of wind stress (b) and SLA (d). Cross-spectral density of both

time series (e). Estimated coherence in blue, phase angle in orange and significant threshold as a dashed line (f). See text for details



Continental Shelf consists of the Brazil, Uruguay, and Argentine Continental Shelves and is the largest continental shelf in the southern hemisphere with exceptionally high biological production (Acha et al. 2004). It is bordered by a steep continental shelf break at the 200 m isobath (Fig. 2). North of  $\sim 35^\circ\text{S}$ , the southern Brazil Continental Shelf is relatively narrow, whereas the continental shelf of Argentina (south of  $35^\circ\text{S}$ ) ranges between 200–800 km and covers most of the study area.

The dominant continental shelf circulation is impacted by the two western boundary currents off the shelf. The equatorward Malvinas current (MC) transports cold water from the northern branch of the Antarctic Circumpolar (ACC) northward along the continental shelf slope, and the Brazil Current (BC) carries warm water from the north. They form the Brazil-Malvinas Confluence at approximately  $38^\circ\text{S}$ , which generates meanders that impact the ocean up to  $45^\circ\text{S}$  (Piola et al. 2001; Gordon 1989; Saraceno et al. 2004), as well as eddies and filaments (Saraceno et al. 2024). On the continental shelf, the circulation shows a similar pattern to the outer shelf circulation, where cold Subantarctic water enters in the south and warm Subtropical Shelf waters are advected from the north. The encounter of the two water masses forms the Subtropical Shelf Front (Piola et al. 2005). North of  $34^\circ\text{S}$ , the continental shelf is characterized by fresh water from the Rio de la Plata. Meltwater from the Pacific enters the continental

shelf at the Magellan Strait and Le Maire Strait and defines the cold and low salinity waters of the southern portion of the continental shelf (Guihou et al. 2020).

The region affected by the Rio de la Plata is characterized by seasonal changing wind directions (Simionato et al. 2005), with the south-westerly winds prevailing during the austral winter, whereas north-easterly winds dominate in summer. Strong westerlies prevail in the southern continental shelf, south of  $43^\circ\text{S}$ .

## 3 Results

### 3.1 Comparison between SLA from altimetry, model, and tide gauges

The SLA were compared to in-situ data from tide gauges obtained from GESLA-3, which were pre-processed to render them comparable to altimetry SLA (see Section 2.1.3). Given the scarcity of continuously available tide gauge measurements during the satellite era, we conducted the analysis whenever tide gauge data were accessible, disregarding any gaps in the data. However, due to the brief duration of the available continuous time data, coherence analysis could not be carried out. Furthermore, it is essential to acknowledge that the absolute values of coherence can only be meaning-

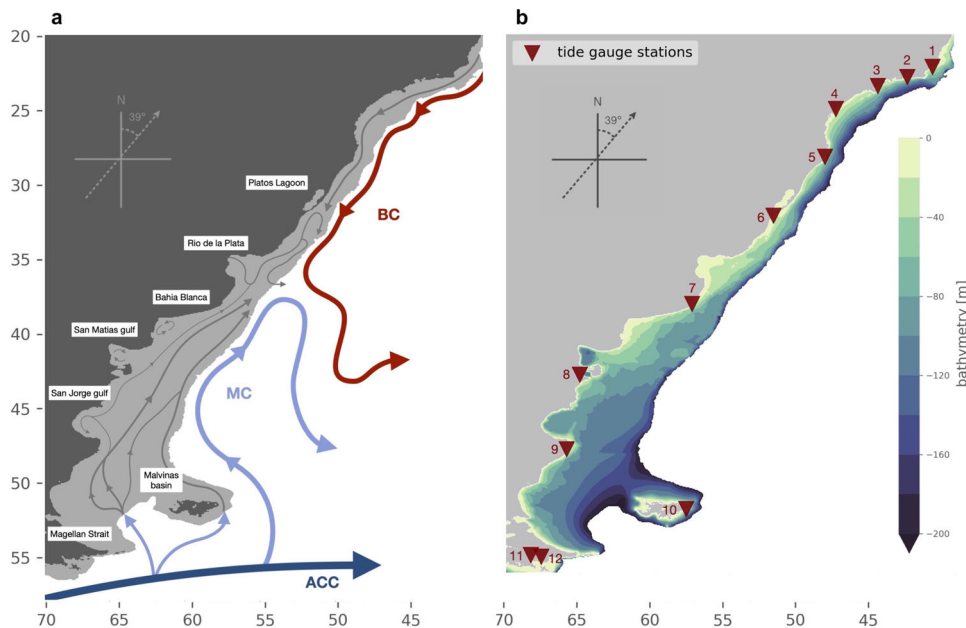


**Fig. 2** Study area of the Southwestern Atlantic Continental Shelf. (a) Schematic of the following main currents: Brazil Current (BC), Malvinas Current (MC), and Antarctic Circumpolar Current (ACC). The continental shelf area (above 200 m isobath) is marked in color by darker grey. Part of the continental shelf circulation is shown by grey arrows, adapted from (Matano et al. 2010). (b) Bathymetry on the continental

shelf (in meters) based on the General Bathymetric Chart of the Ocean (GEBCO, 2003), combined with the bathymetry measurements from Servicio de Hidrografía Naval (SHN, Argentina). Tide gauge locations are shown in red. Site names according to site numbers can be found in Table 1. Latitude given in  $^\circ\text{S}$  and longitude in  $^\circ\text{W}$

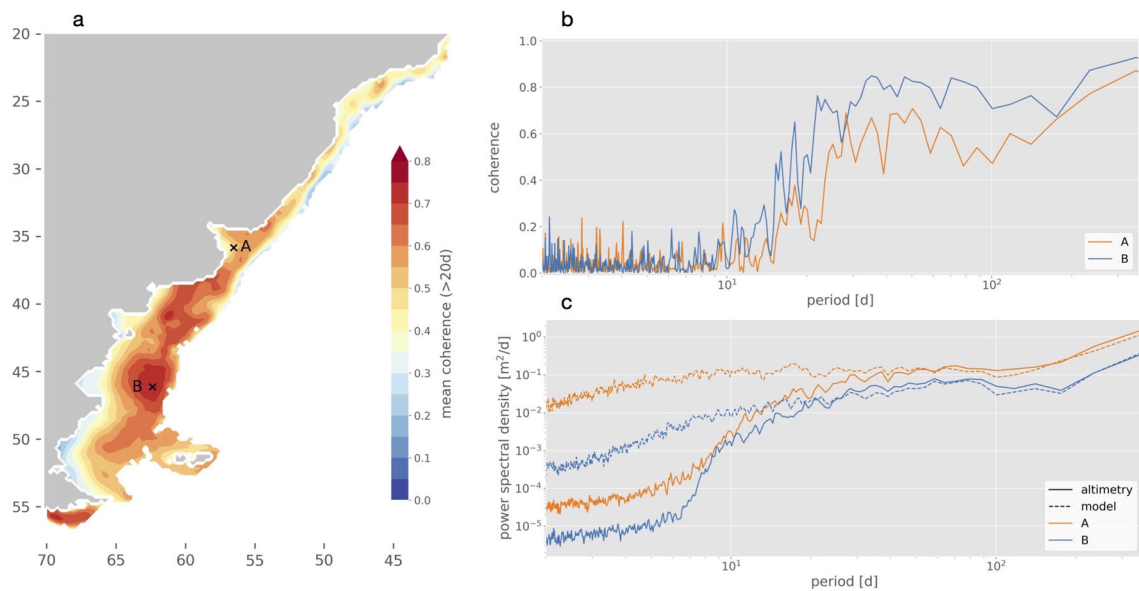
fully compared when the same conditions, such as the length of all time series, are employed.

Table 1 shows the correlation coefficients between SLA derived from tide gauge data compared with altimetry-based SLA ( $corr_{alt}$ ) and with model SLA ( $corr_{mod}$ ).  $corr_{mod}$  was higher at every station than  $corr_{alt}$ , showing that the model compares better with the tide gauge SLA than the altimetry product. The highest correlation reached between the model and tide gauge SLA is at Puerto Madryn (0.93), where altimetry and tide gauge had the lowest agreement (0.18). The model SLA show more variability, whereas gridded altimetry SLA seem unable to reproduce SLA coastal variability.  $corr_{alt}$  achieved its lowest values for the southernmost stations, Ushuaia and Puerto Williams. Gridded altimetry compared better with tide gauge SLA for the stations north of 42°S as well as Port Stanley, which is not located along the central coastline, but east of the Malvinas islands.

We then compared the gridded SLA used in this study with SLA obtained from a model from 1993 to 2019 using coherence analysis. Figure 3a shows the mean coherence for periods of > 20 d. The mean coherence suggests that the model data and the altimetry data agree (mean coherence > 0.5) along the entire continental shelf between 34 and 42°S and south of 55°S (Fig. 3). North of 34°S, the coherence values ranged between 0.35 and 0.5 close to the coast and are lower than 0.3 towards the continental shelf break. Between 40°S and 55°S, we found a relatively low agreement of 0.35 at the coast, with increasing coherence farther from the coast. The highest agreement between the model and altimetry SLA

(> 20 d) was found on the continental shelf between 38°–52°S. The coherence was also significantly high on the coast south of the Rio de la Plata estuary. In contrast, the agreement between the model and altimetry SLA decreases below significance on the southern coastline. The maximal coherence (> 0.75) was obtained in the mid-southern Patagonian continental shelf (marked by B). On the northern part of the study area (north of 35°S), the agreement is low (< 0.28) along the continental shelf break (200 m isobath), while coherence remains above significance (0.4–0.55) towards the coastline. Considering the coastal zone, by combining these results with the comparison of the model and tide gauge SLA (Table 1,  $corr_{model}$ ), we can conclude that the altimetry gridded data have issues in representing the variability along the coast of the southern part of the domain, while a better agreement among the three data sources is found in the rest of the domain.

Figures 3b and c provide additional insights into the differences between the model and altimetry SLA per period (1/frequency), at two the locations shown in Fig. 3a. Both locations, A (Rio de la Plata estuary) and B (mid-southern continental shelf) are the subjects of further analysis in this section. We found the most significant sub-annual coherence values at ~50 d in the Rio de la Plata estuary (A) and 30–80 d (plateau-like) for the mid-continental shelf (B). The power spectral density (PSD) reveals the energy perspective of this comparison. Both analysis show a higher energy content at all temporal scales for A, which matches the higher sea level variance in the coastal zone compared to the open shelf areas reported in Fig. 12. Generally, the model shows more energy



**Fig. 3** Comparison of altimetry- and model-based SLA. (a) Mean coherence between model and altimetry SLA over continental shelf within study domain. (b) Coherence of SLA at the two locations depend-

ing on the period. (c) power spectral density (PSD) of altimetry (solid line) and model (dashed line) SLA at the selected locations. Latitude given in °S and longitude in °W

than altimetry at both locations. In particular, gridded altimetry strongly suppresses the energy content for periods below three months. This is a notable result since previous studies, considering the effective temporal resolutions of the altimetry maps, estimated this to be about 14–21 d in our study domain and 34 d as a global mean (Ballarotta et al. 2019). Our analysis suggests that the optimal interpolation to generate these grids likely suppresses part of the signal at much higher frequencies.

### 3.2 Coherence between SLA and wind

Given the dominant role of the along-shore wind stress component (see Section 2.2) we studied the coherence between SLA and the along-shore wind stress component to gain deeper insights into continental shelf processes. To do so, we performed a coherence analysis of the time series from Jan. 1993 to Dec. 2019 using satellite (L4) and model with the along-shore wind stress (Section 2.1) at each grid point. The coherence was analyzed within bands from 20 to 234 d and for the annual period. For completeness, it is worth noting that the across-shore wind stress component showed signifi-

cantly less coherence with the SLA on sub-annual scales (not shown).

#### 3.2.1 Altimetry SLA and along-shore wind

The coherence between SLA from altimetry and along-shore wind stress component is shown in Fig. 4. One can easily observe from the Figure that the agreement between SLA and the along-shore wind stress is higher on the shelf than in the rest of the domain. It is known, due to the combination of continental shelf topography, Ekman transport, and upwelling/downwelling processes, that the influence of the wind on sea level is more pronounced and localized on the continental shelf than outside the shelf in deeper oceanic regions. Significant agreement with altimetry SLA (coherence > 0.32) was obtained for the along-shore wind stress component in periods > 50 d on portions of the continental shelf.

Annually, SLA and along-shore wind stress are coherent along the entire continental shelf except for latitudes < 50°S where the coastline changes orientation (Fig. 4, annual) and towards the 200 m isobath north of 33°S. Coastal regions

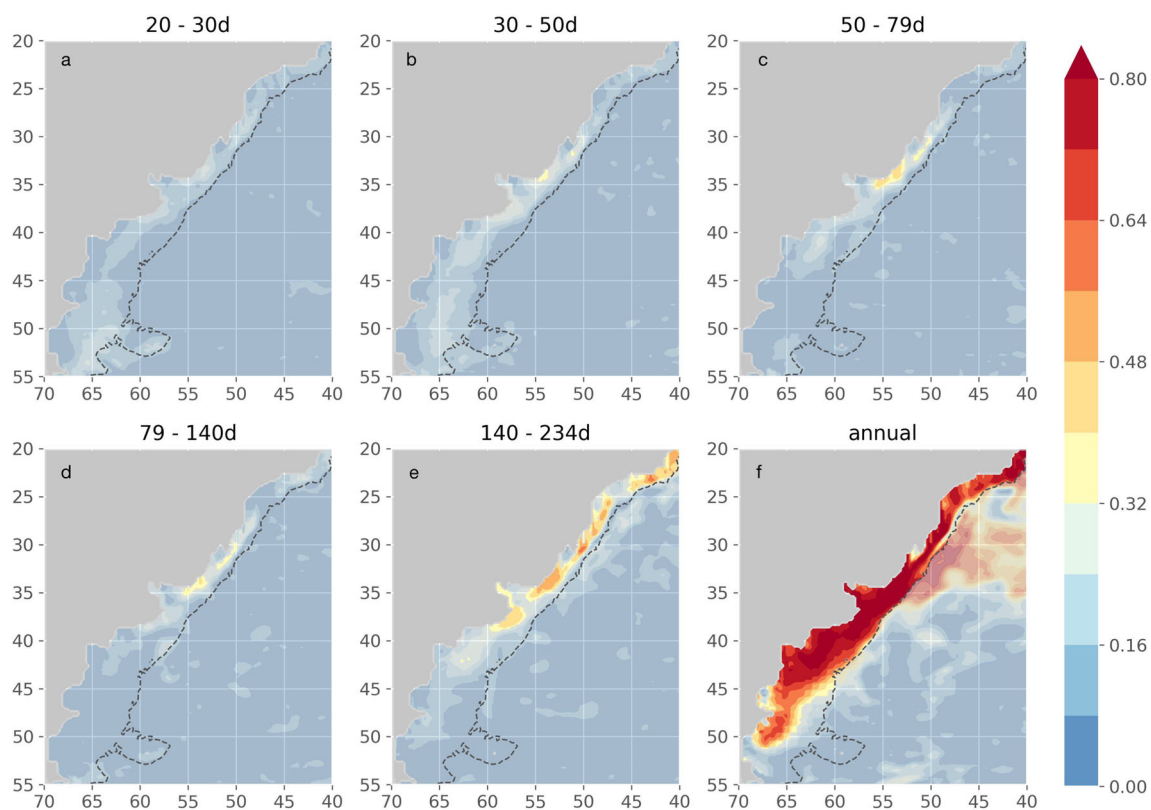


**Fig. 4** Mean coherence between SLA from altimetry and along-shore wind stress over selected frequency bands: (a) 1/20 d - 1/30 d (b) 1/30 d - 1/50 d (c) 1/50 d - 1/79 d (d) 1/79 d - 1/140 d, (e) 1/140 d - 1/234 d and

(f) annual. The 200 m isobath is indicated as a dashed line. Significant coherence on the continental shelf is visible in regular color, while the others are in semi-transparent. Latitude given in °S and longitude in °W



showed lower coherence near large river mouths (e.g., Rio de la Plata, 35°S and 56°W). South of 50°S, no significant agreement between SLA and the along-shore wind stress was obtained over the frequency bands.

In the frequency band of 1/140 d - 1/234 d, coherence between along-shore wind stress and SLA shows significant agreement on the continental shelf north of 50°S. The values there were lower than in the annual period. The highest agreement in the band of 1/140 d - 1/234 d was obtained along the continental shelf north of ~ 36°S, e.g., in the Rio de la Plata estuary and northwards connected continental shelf, with values reaching 0.56. At the coast, along-shore wind stress and SLA had notable low coherence and, below significance for larger land inlets, e.g., San Matias Gulf at ~41°S and San Jorge Gulf at ~46°S in the periods 140-234 d.

Considering temporal scales below the semi-annual period (20-30 d, 30-50 d, 50-79 d, and 79-140 d), significant coherence remains visible onshore, mainly north of the Rio de la Plata estuary along a narrow coastal band. For periods > 50 d, a significant coherence remained visible at the northern part of the Rio de la Plata estuary (between 34-35°S). In the highest frequency band (20-30 d), we observed no signifi-

cant coherence with the along-shore wind stress using the altimetry SLA.

### 3.2.2 Model SLA and along-shore wind

In Fig. 5, the same coherence analysis is performed as in Fig. 4, using model SLA instead of gridded altimetry. There is a notable agreement between the two Figures, showing the same areas of strong coherence between SLA and along-shore wind on the continental shelf in the annual period. A mean coherence above 0.8 covered the entire continental shelf width for > 50°S, comparable with the coherence obtained using altimetry SLA, showing similar exceptions for gulf areas (~46°S) and close to the continental shelf break > 31°S latitudes. For 140-234 d, the most considerable coherence achieved in the band was also found along the continental shelf between 25-35°S, but with notable larger values of up to 0.64.

More differences were visible in the higher frequencies (20 to 140 d) in magnitude. The model data showed a higher coherence than altimetry in the coastal band north of Rio de la Plata. The most significant differences are observed in

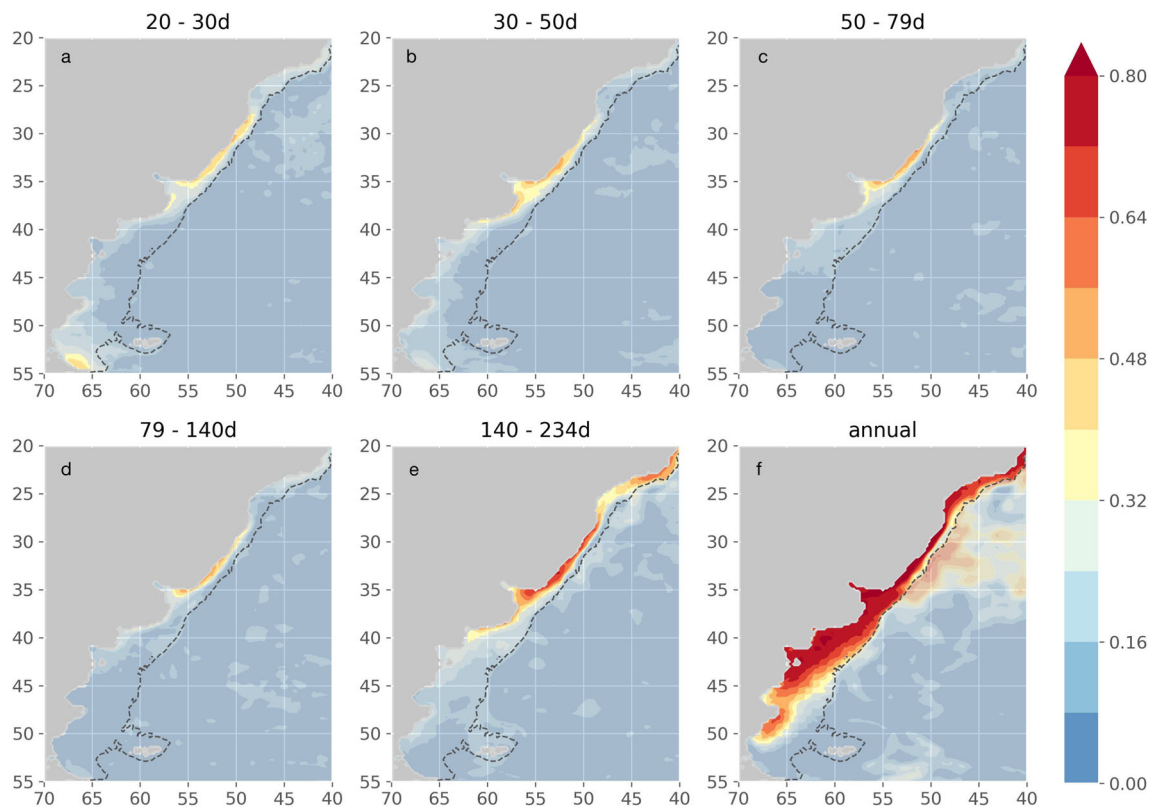
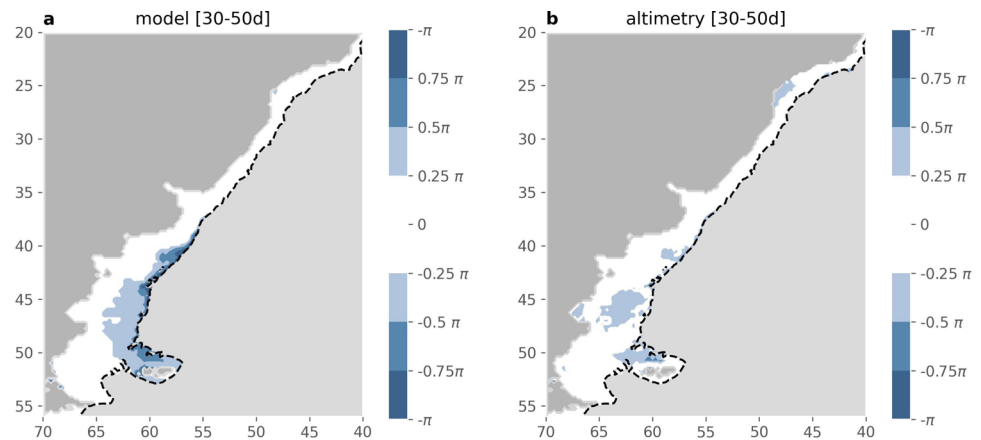


**Fig. 5** Mean coherence between SLA from numerical model and along-shore wind stress over selected frequency bands: (a) 1/20 d - 1/30 d (b) 1/30 d - 1/50 d (c) 1/50 - 1/79 d (d) 1/79 d - 1/140 d, (e) 1/140 d - 1/234 d and (f) annual. The 200 m isobath is indicated as a dashed line. Signifi-

cant coherence on the continental shelf is visible in regular color, while the others are semi-transparent. Latitude given in °S and longitude in °W

**Fig. 6** Phase angle of SLA and along-shore wind stress for the periods 30–50 d corresponding to coherence estimations shown in Figs. 4b and 5b. Phase angle shown on the continental shelf. Latitude given in °S and longitude in °W



the higher level of coherence between the model and along-shore wind stress at 20–30 d and 30–50 d, which shows that the gridded altimetry is less coherent than the model with the along-shore wind stress at this temporal scales. In particular, when comparing Fig. 4 with Fig. 5, we observe higher coherency at the same frequencies where we have previously observed a higher power spectral density (PSD) in the model (Fig. 3c). This suggests a missing wind-driven signal in the altimetry maps.

### 3.2.3 Considerations of the phase

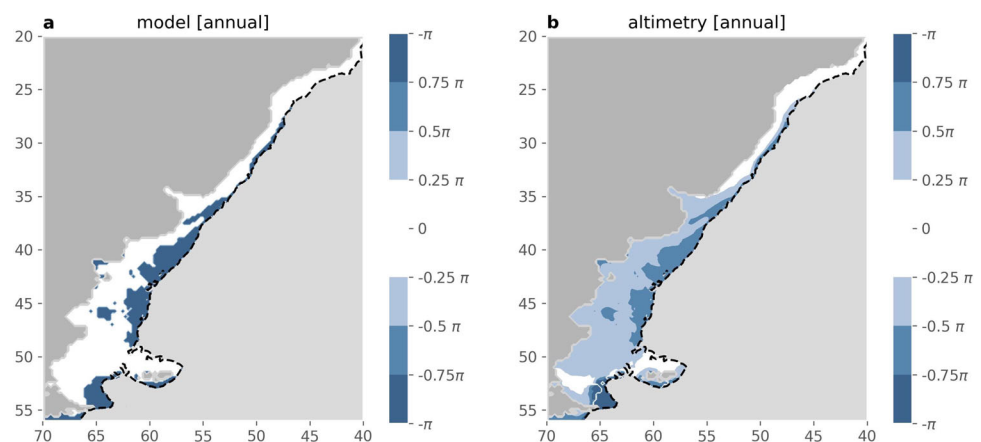
In addition to the coherence analysis, we consider potential phase lags between the wind stress and SLA analyzed in this study. We use the cross-spectral density, a coherence constituent (see Eq. 6). As mentioned in 2.2, the cross-spectral density is a complex quantity and contains phase information in its imaginary part. This derived phase holds meaningful interpretation only where coherence gains significance (Thomson and Emery 2014; Eriksson 1970).

The Fig. 6 shows the phase shift for the sub-annual band (30–50 d). The main result is that both altimetry and model observe no phase shift between along-shore wind stress and

SLA at sub-annual scales on the locations where the two are significantly coherent, here shown for the 30–50 d period ( $< 0.25 \pi$  correspond to  $< 5$  d for 30–50 d period). The result suggests a direct response in the SLA to the along-shore wind stress forcing in this period.

Model and altimetry SLA show differences in the phase shift with the along-shore wind stress for annual periods (Fig. 7). In both cases, northward of  $35^\circ\text{S}$ , the phase angles are below  $0.25 \pi$ , whereas more to the South, the phase lag considering altimetry SLA is up to  $0.25$ – $0.5 \pi$ , which corresponds to three to six months. However, both model and altimetry show larger values close to the shelf-break, whereas the model values are larger than altimetry values. The pattern might be due to the fact that in this region, SLA are affected by the boundary currents and not by the along-shore wind stress. We note that the low phase shift between altimetry SLA and along-shore wind stress matches the area of prevailing along-shore winds of Fig. 12, while the phase shift increases towards the south, where westerlies prevail. Nevertheless, the significant phase lags derived from the satellite SLA indicate that, at the annual period, the SLA south of  $35^\circ\text{S}$  do not directly respond to local along-shore wind stress forcing. This observation differs from the model simulations

**Fig. 7** Phase angle of SLA and along-shore wind stress for the annual period corresponding to coherence estimations shown in Figs. 4f and 5f. Phase angle shown on the continental shelf. Latitude given in °S and longitude in °W



for the inner continental shelf. Still, it agrees with the fact that the MC affects the continental shelf region close to the shelf-break, as suggested by Matano and Palma (2018) and quantified by Lago et al. (2021) at 41°S.

### 3.2.4 Geostrophic velocity from altimetry and wind

In Fig. 8, we present a coherence analysis similar to the previous examples but explicitly focusing on the relationship between the along-shore component of the wind stress and of the geostrophic velocity. The along-shore flow primarily influences the circulation on the continental shelf, and therefore we specifically consider the along-shore component of the geostrophic velocity. It is important to note that this analysis is not entirely independent of the one depicted in Fig. 4 because the geostrophic velocities are directly derived from the gridded SLA (Section 2.1). Coherence above 0.8 was observed along the continental shelf between 20–36°S, particularly considering the annual period. Wind variability is likely to cause a pressure gradient by affecting the SLA on the continental shelf. This results in a velocity change through geostrophic adjustment. Therefore, the agreement

between geostrophic velocities and along-shore wind stress dominates annually since the wind variability has a significant annual cycle, as described previously (e.g., Saraceno et al. 2014). We observe a coherence of up to 0.56 along the shelf from 25–35°S for the semi-annual band. For > 50 d, significant coherence can be noticed in this area intermittently. In accordance with the previous section, no significant agreement is recognized below 50 d for the altimetry-based data.

### 3.2.5 Geostrophic velocity from model and wind

Similar to the coherence analysis of the satellite SLA, we compare the geostrophic part of the model surface velocity with the along-shore wind stress. We obtain a few similarities by comparing these results with Fig. 8: The annual coherence reaches the highest value of > 0.8 north of the Rio de la Plata. The model shows a more extended high-coherence area over the whole shelf width and further in the southern direction (~45°S). In particular, the two areas of high coherence north and south of Rio de la Plata correspond to the pattern of the northward/ southward continental shelf currents reported in

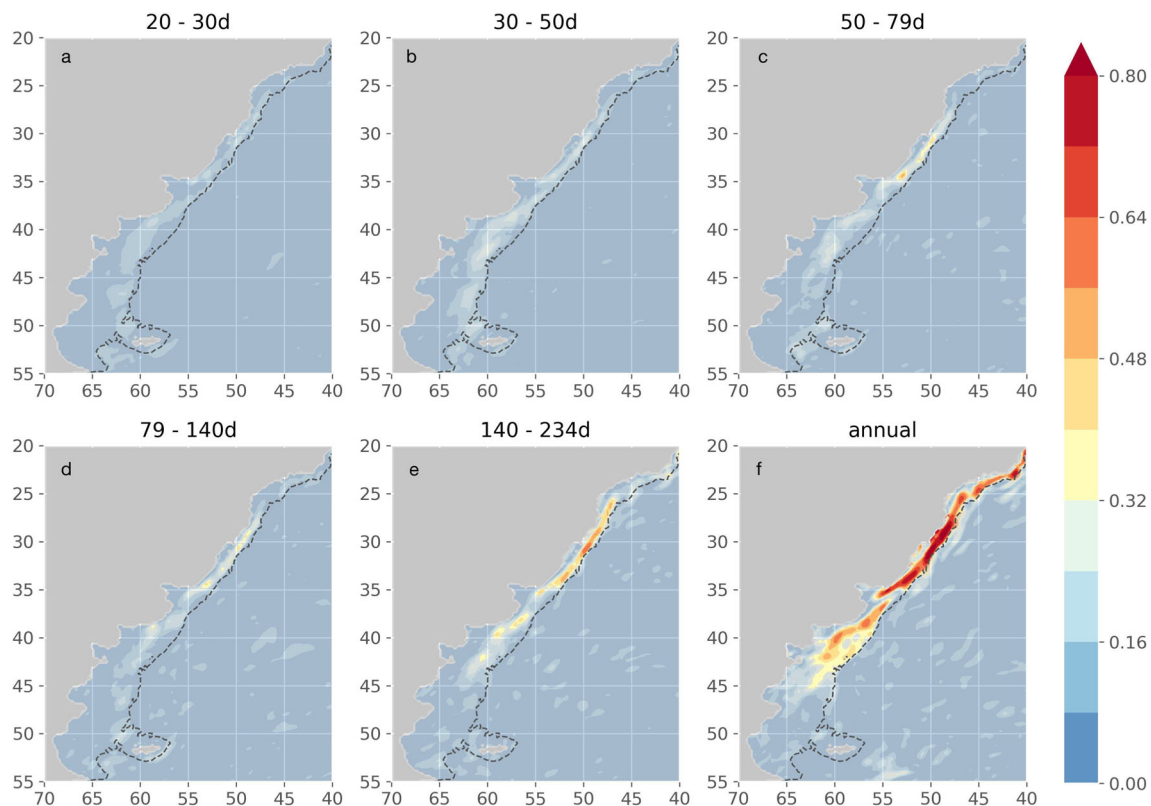


**Fig. 8** Mean coherence between along-shore geostrophic velocity from altimetry and along-shore wind stress over selected frequency bands: (a) 1/20 d - 1/30 d (b) 1/30 d - 1/50 d (c) 1/50 d - 1/79 d (d) 1/79 d - 1/140 d, (e) 1/140 d - 1/234 d and (f) annual. The 200 m isobath is indicated as

a dashed line. Significant coherence on the continental shelf is visible in regular color, while the others are semi-transparent. Latitude given in °S and longitude in °W

Section 2.3. Also, for the semi-annual band, 140–234 d, we note a robust alignment north  $\sim 35^\circ\text{S}$  with the velocities from altimetry, although also, in this case, the model has higher coherence. More noteworthy is the disagreement for periods below 140 d. The velocities from the model show significant agreement with the wind stress for all periods within  $28\text{--}42^\circ\text{S}$  and toward the coast. At the same time, in Fig. 9, there was no significant coherence south of the Rio de la Plata estuary.

### 3.3 EOF analysis

In the previous subsection, we have described the coherence between wind stress and SLA over parts of the Southwestern continental shelf, even for periods shorter than annual and semi-annual cycles. In this part, we conducted an EOF analysis to decompose the SLA signals from altimetry and model to investigate the potential influence of the along-shore wind stress. The EOF analysis was performed on regions on the continental shelf to exclude open ocean processes. We infer sub-annual scales from the first two modes through coherence

on selected frequency bands rather than filtering the original data based on the abovementioned methods. For sub-annual scales, we selected the 20–79 d band, corresponding to the first three bands used in the previous analysis. Since, as previously shown, the SLA from altimetry does not represent scales of variability below 20 d, we applied a 20d-lowpass Butterworth filter of the first order to the model SLA to make the EOF comparable to the ones of the gridded altimetry SLA (for details, see Figs. 13 and 14).

The first EOF mode, which explains 43.0% of the variance for gridded altimetry and 64.5% for the model, shows a monopole concentrated around the Rio de la Plata estuary and the adjacent coast. The first EOF shows similar pattern for altimetry and model ( $\text{corr} = 0.90$ ), with highest variance in the region of large river runoffs and seasonally changing wind direction, showing the dominant annual signal present in this mode (see Figs. 15 and 16, a topic already explored in various publications e.g., Ruiz Etcheverry et al. 2016).

The coherence of the reconstructed SLA from the first mode and along-shore wind stress shown on the sub-annual scales 20–79 d in Figs. 10e and 11e reveal low agreement

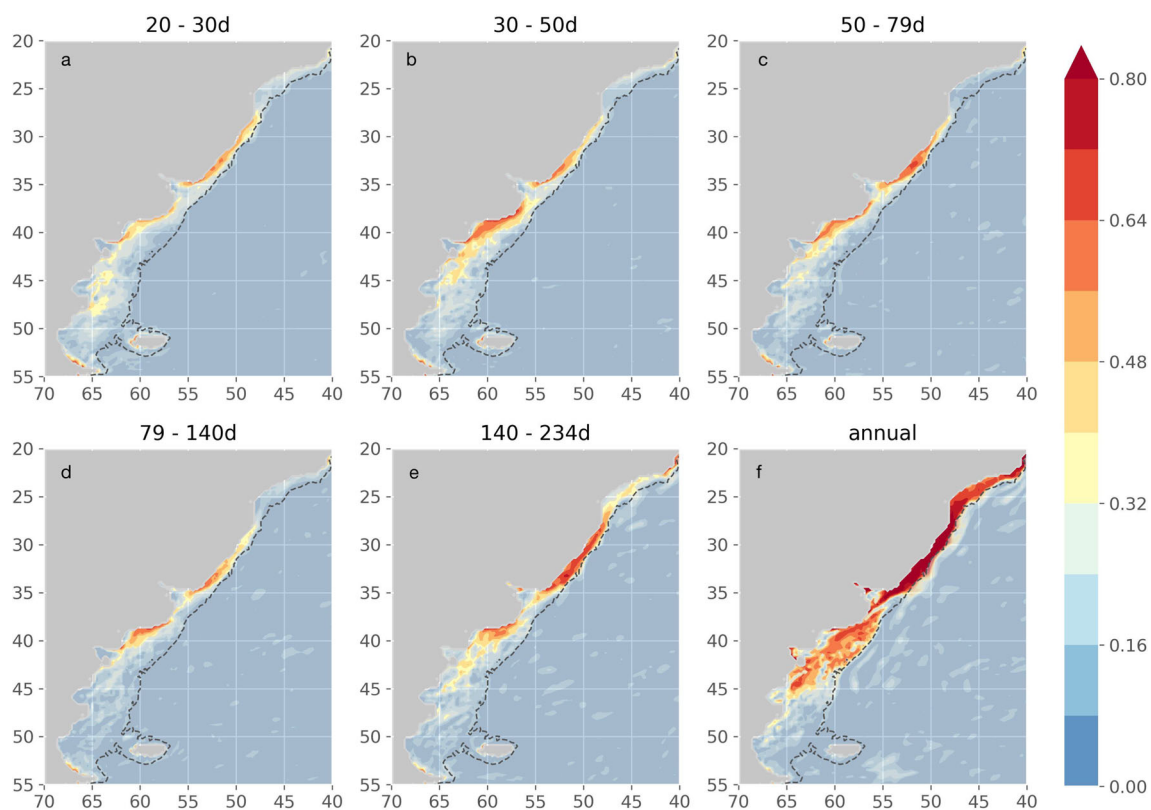
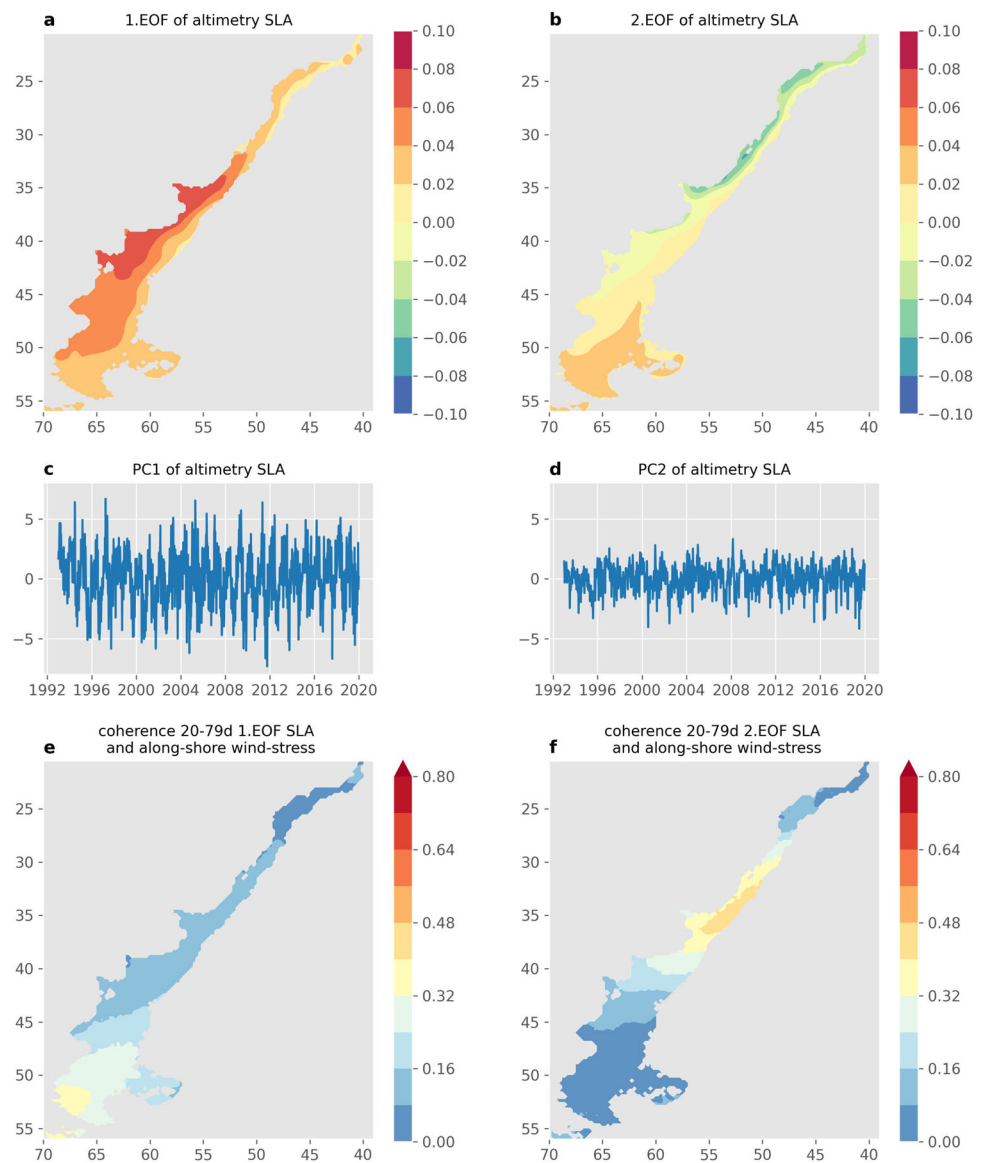


**Fig. 9** Mean coherence between along-shore geostrophic velocity from altimetry and along-shore wind stress over selected frequency bands: (a) 1/20 d - 1/30 d (b) 1/30 d - 1/50 d (c) 1/50 d - 1/79 d (d) 1/79 d - 1/140 d, (e) 1/140 d - 1/234 d and (f) annual. The 200 m isobath is indicated as

a dashed line. Significant coherence on the continental shelf is visible in regular color, while the others are semi-transparent. Latitude given in  $^\circ\text{S}$  and longitude in  $^\circ\text{W}$



**Fig. 10** EOF analysis of altimetry SLA: (a) First and (b) second EOF eigenvectors over the continental shelf and corresponding principle components in (c) and (d). Mean coherence between 20-79 d of reconstructed SLA with along-shore wind stress for first (e) and second (f) EOF mode. Latitude given in °S and longitude in °W



almost over the whole shelf except in the southernmost area of the continental shelf (51-54°S). Here, a significant coherence of 0.32 is estimated, coinciding with an area where wind stress has seasonally increased variance (Fig. 12). Nevertheless, the spatial pattern of the first EOF has a lower amplitude in this region relative to the center of the monopole between 30-42°S (Figs. 10a and 11a).

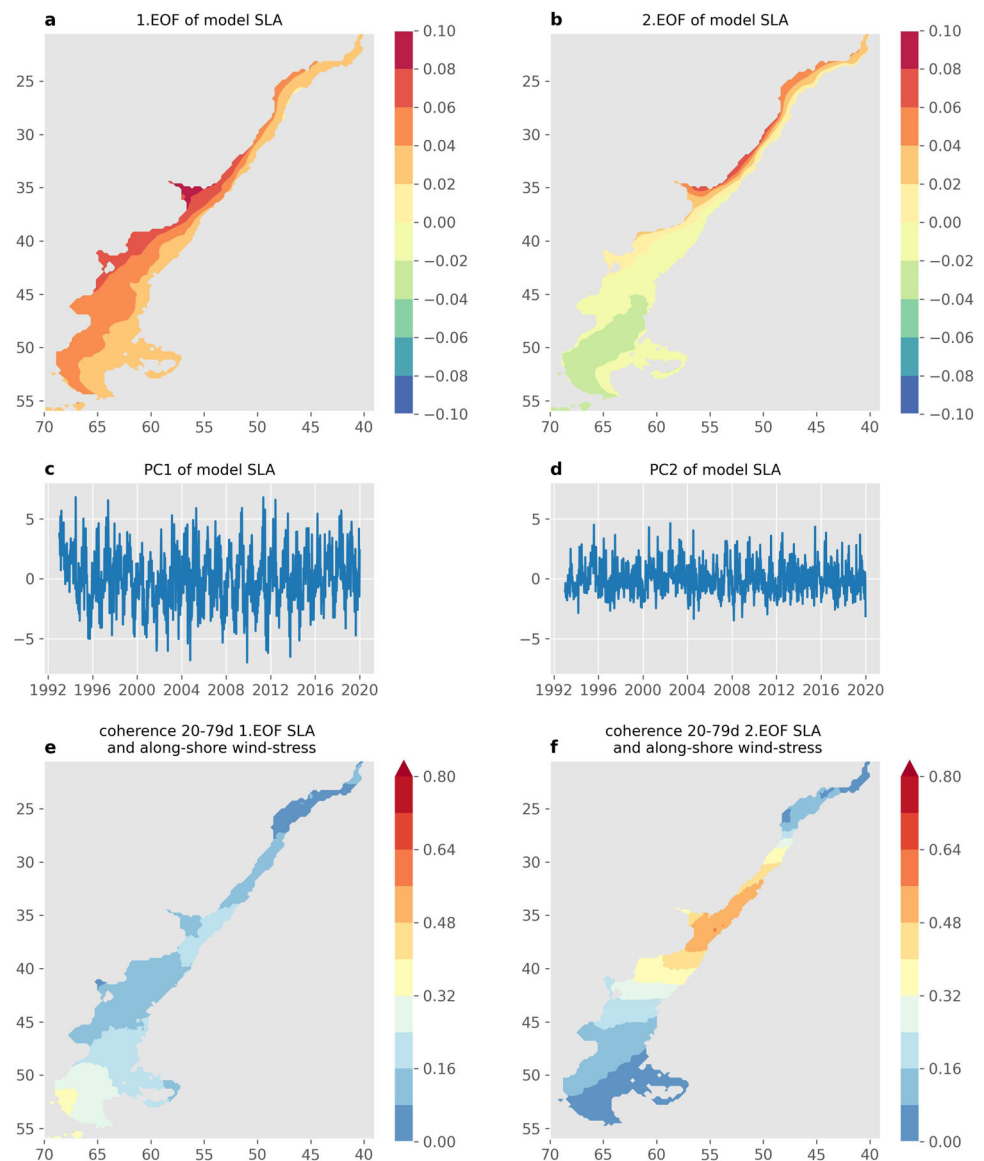
The second EOF shown in Figs. 10b and 11b has a dipole character, again with a high agreement between the EOF-pattern from altimetry and model (corr = 0.96). This EOF mode also has a significant annual cycle (see Figures 15 and 16), while the reconstructed SLA show significant coherence with the along-shore wind stress in the high-frequencies investigated: Between 20 and 79 d, notable coherence is evi-

dent in Figs. 10f and 11f, spanning from 27-38°S for altimetry and 27-40°S for model SLA from second EOF, respectively, across the entire continental shelf width. The second EOF mode accounts for 10.7% variability of the total SLA signal for altimetry and 18.1% for model data, respectively. In contrast to the first mode, the dominant spatial pattern amplitude aligns with the region of significant coherence with the wind stress.

The first and second EOF modes from SLA agree well with previously shown EOF patterns in the study region, e.g., by Combes and Matano (2018). Significant coherence found for the first EOF SLA in the southern part of the study region has been linked before by Combes and Matano (2019) partly to a modulation through local wind variability. In addi-



**Fig. 11** EOF analysis of 20d-lowpass-filtered model SLA: (a) First and (b) second EOF eigenvectors over the continental shelf and corresponding principle components in (c) and (d). Mean coherence between 20-79 d of reconstructed SLA with along-shore wind stress for first (e) and second (f) EOF mode. Latitude given in °S and longitude in °W



tion, we have found that the coherence between along-shore wind stress and SLA at sub-annual scales is connected to the second EOF mode, which accounts for 10.1% (altimetry) to 18.7% (model) of the total SLA variability.

#### 4 Summary of results and discussion

In this work, we have analyzed the sea level variability and its connection with the along-shore wind stress on the Southwestern Atlantic Continental Shelf. We used gridded altimetry, a numerical model from CMEMS, and tide gauge data to verify this. Although tide gauges provide precise

measurements, their record in our study area is sparse and discontinuous. Consequently, the analysis against tide gauges was limited to correlating their time series with other data sources. However, from this analysis, we gained an important insight: the numerical model showed a better correlation with the tide gauges than the altimetry data. This strong correlation between the model and tide gauges allowed us to use the model as a reliable reference to test the performance of the SLA from gridded altimetry data. This cannot be done using only the tide gauges, as they provide point measurements. By examining the power spectral density of the SLA, we found that altimetry data exhibited similar behavior to the model for scales longer than the semi-annual period but lower magnitudes of the sea level variance at shorter

periods. It is important to note that the limited representativeness of gridded altimetry at high frequencies is well known. Below 20 d, this limitation is due to the application of the Dynamic Atmosphere Correction (DAC), which aims to remove high-frequency variability caused by wind-related effects. The current altimeter constellation does not adequately capture these effects due to sampling issues. Similar findings were reported in our study area by Ferrari et al. (2017) and Lago et al. (2021), who demonstrated that the best correlation between gridded altimetry and in-situ measurements was achieved using a 20 d-lowpass filter on the gridded data. Furthermore, Ballarotta et al. (2019) discussed the effective resolution of gridded altimetry products, suggesting representativeness for periods longer than 14–21 d in our study region. Since the model showed a better correlation with the tide gauge data than altimetry and has proven to have more energy on periods even higher than the reported effective resolution, we suggest that gridded altimetry may underestimate the high-frequency signal. Beyond that, we conclude that gridded altimetry data have issues representing the variability along the coast and in the southern part of the study region. The limitations encountered by altimetry data in representing the high-frequency variability, particularly near the coast, and the dominant influence of SLA from local winds in coastal areas may explain the better correlation of the numerical model (forced by atmospheric reanalysis) with tide gauges compared to altimetry data. We analyzed the coherence and decomposed the signals using Empirical Orthogonal Functions (EOFs). Our main finding is that the coherence between along-shore wind stress and SLA is significant for a large part of the study domain, even for periods shorter than the annual and seasonal signals. This finding expands on previous publications, such as Simionato et al. (2006); Meccia et al. (2009); Strub et al. (2015); Saraceno et al. (2014). We observed that altimetry maps can identify wind-related variability, as evident in the same regions using both sea level datasets. However, the coherence between the altimetry SLA and along-shore wind stress significantly decreases compared to the model data for sub-annual periods, particularly  $< 50$  d. Furthermore, upon examining the surface geostrophic velocity component of both altimetry and model-based data, it becomes evident that altimetry fails to capture a portion of the wind-related modulation affecting the shelf flow. More precisely, along-shore wind-driven SLA contribute to the across-shore pressure gradient, causing along-shore velocity anomaly by geostrophic adjustment. This is a known process, measured with in-situ data in a part of the study region, e.g., by Lago et al. (2019). On annual scales, we find the highest coherences between along-shore wind stress and SLA; coherence could arise from the shared

dominant periodicity on the annual scale. This is supported by previous studies that found solar radiation and connected steric height changes to be the main source of sea level changes on the annual scale south of  $36^{\circ}\text{S}$  (Ruiz Etcheverry et al. 2016), while north of  $36^{\circ}\text{S}$  wind is the main responsible for annual SLA (Saraceno et al. 2014).

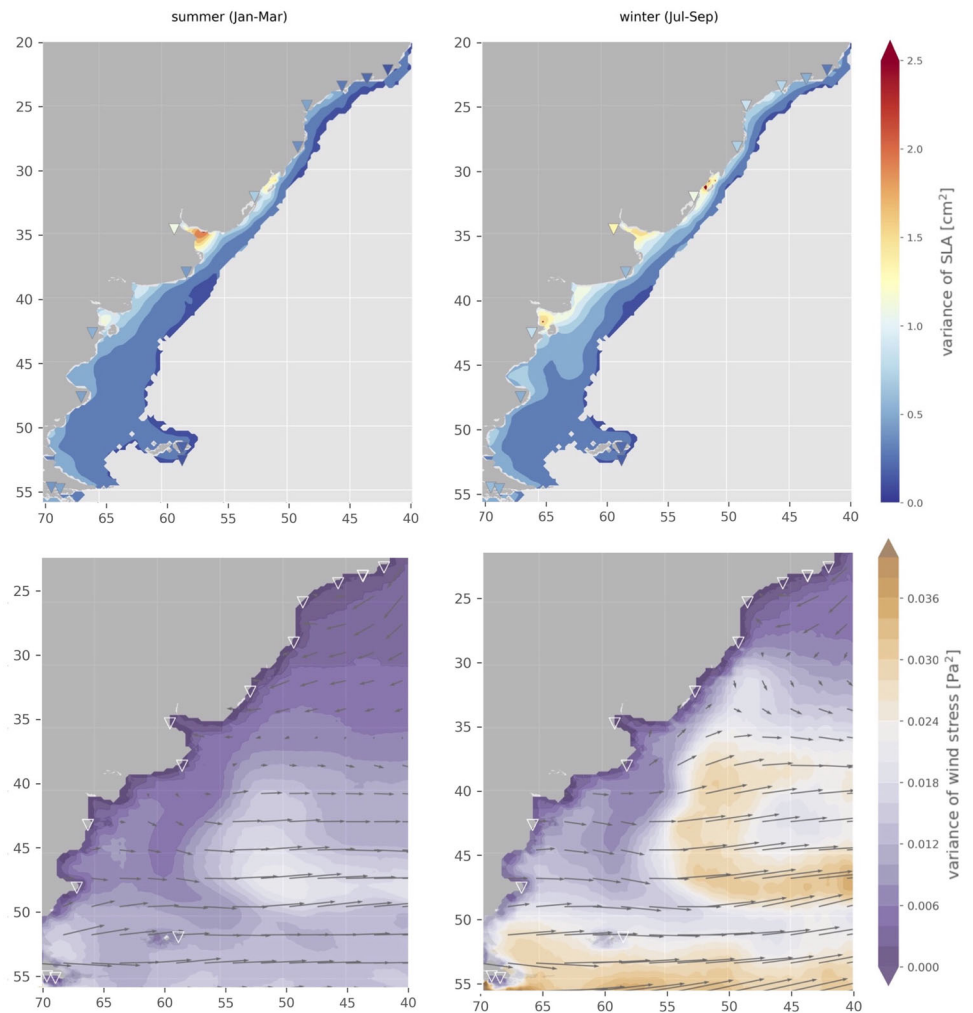
While coherence indicates whether two signals correlate within specific frequency bands, it does not quantify the contribution of a specific driver to the overall variability. An EOF analysis of the SLA revealed that the second principal component explains a similar fraction of the variability for altimetry and model SLA and showed the largest agreement with the along-shore wind stress.

The strong coherence of the model with wind stress at sub-annual periods leads us to conclude that the current altimetry maps in the Southwestern Atlantic Continental Shelf do not adequately represent high-frequency sea level variability compared to the model. Specifically, they have a lower wind-driven signal than the model at longer temporal scales than expected based on the common effective time resolution (Ballarotta et al. 2019). We consider the combined use of EOF and coherence analysis as an important contribution of this study. This approach can be applied to investigate wind as a driver of sea level variability and, specifically, to assess the mapping capabilities of altimetry-based products in other continental shelf areas of the global ocean. Many studies rely solely on correlation-based analysis, which tends to overlook sub-annual variability in favor of stronger signals at annual to interannual scales.

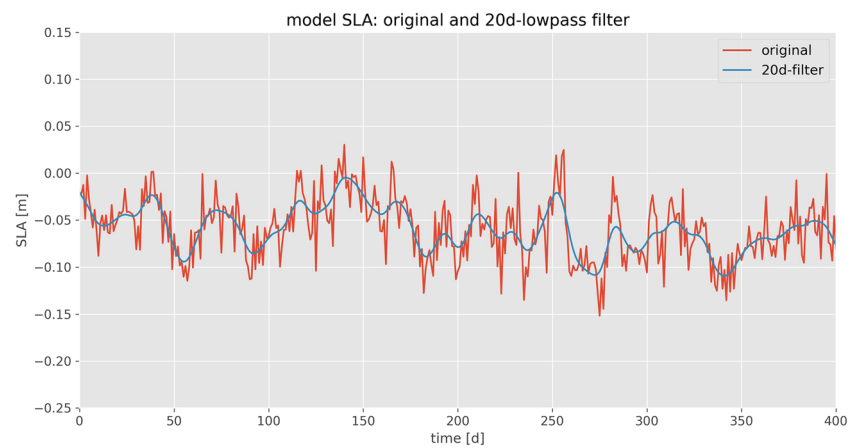
The smoothing and filtering methods applied in the optimal interpolation underlying CMEMS altimetry maps likely play a role in the missing signal observed in dynamic areas like the Southwestern Atlantic Continental Shelf. These maps are generated using the same methodology regardless of the study region, whether open ocean, shelf, or coastal areas. Passaro and Juhl (2023) demonstrated that machine learning techniques can potentially improve the temporal content of these maps. Machine learning methods are particularly suitable for integrating predictors from external datasets, and considering the insights gained from this study, wind stress should be considered as a predictor. Enhancing the description of temporal scales is crucial, especially with the new SWOT mission launched in 2022, which is expected to significantly improve the spatial resolution of sea level maps. Preliminary efforts to merge SWOT data with CMEMS maps are underway (Beauchamp et al. 2023). However, since the SWOT orbit has a repetition time of 21 d, exploiting and improving the temporal content of gridded maps is crucial to fully benefit from this new era of satellite altimetry observations.

## Appendix A

**Fig. 12** Variance of altimetry SLA (top) and wind stress (bottom) over austral summer (left) and winter (right) from 1993 - 2019. Inverted triangles show the daily, 40h-Loess-filtered SLA variance from tide gauge data. Arrows indicate the mean wind direction. Latitude given in °S and longitude in °W



**Fig. 13** Time Series from model SLA. Original and 20 d-lowpass filtered using Butterworth filter at one point (64.875°S, 51.875°W)



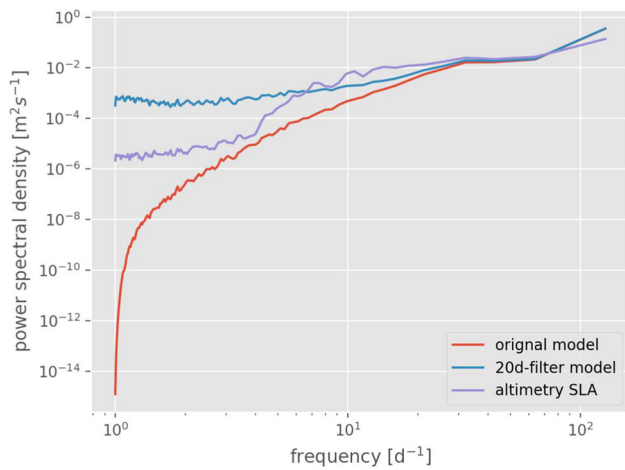


**Fig. 14** Power spectral density from model and altimetry SLA. Original and 20 d-lowpass filtered model SLA using Butterworth filter shown in comparison with altimetry SLA at one point (64.875°S, 51.875°W)

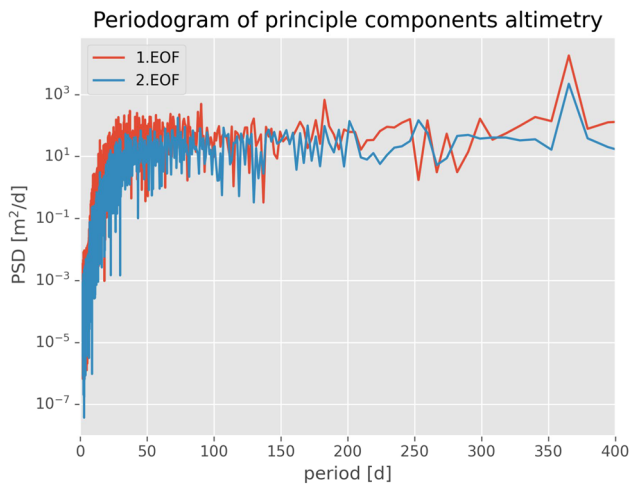


**Fig. 15** Periodogram of principle component from the first and second EOF mode from altimetry SLA shown in Fig. 10

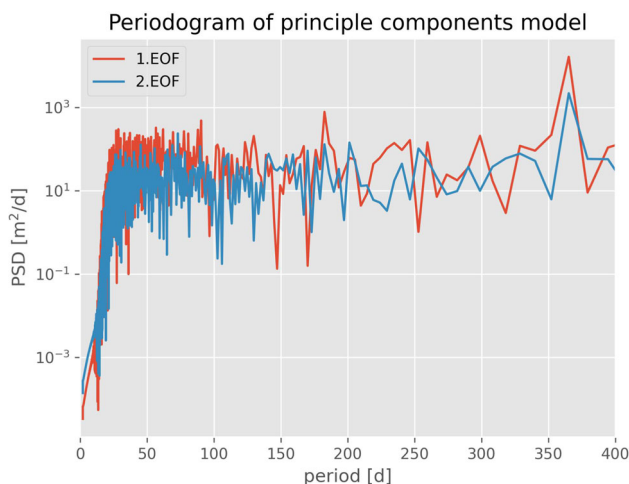


**Fig. 16** Periodogram of principle component from the first and second EOF mode from 20d-lowpass-filtered model SLA shown in Fig. 11

**Acknowledgements** This study is part of the DFG-funded project CIRCOS (PA3111/7-1, Project Number 450008353) at Deutsches Geodätisches Forschungsinstitut der Technischen Universität München (DGFI-TUM) and EUMETSAT/CNES Project SABIO. The authors thank the anonymous reviewers and Nicolás Bodnariuk for their valuable comments and suggestions on this manuscript.

**Funding** Open Access funding enabled and organized by Projekt DEAL.

**Data Availability** The gridded altimetry, model, and wind data used in this study are distributed by E.U. Copernicus Marine Service Information. Gridded altimetry Sea Level Anomalies are available under: <https://doi.org/10.48670/moi-00148> (accessed 05/2022), model SSH can be found at <https://doi.org/10.48670/moi-00021> (accessed 09/2022) and the wind stress is provided as components under: <https://doi.org/10.48670/moi-00305> (accessed 06/2022). Bathymetry data are based on the General Bathymetric Chart of the Ocean (GEBCO, 2003) and the bathymetry measurements from Servicio de Hidrografia Naval (SHN, Argentina).

**Declarations**

**Conflicts of interest** The authors declared that they have no conflict of interest.

**Open Access** This article is licensed under a Creative Commons Attribution 4.0 International License, which permits use, sharing, adaptation, distribution and reproduction in any medium or format, as long as you give appropriate credit to the original author(s) and the source, provide a link to the Creative Commons licence, and indicate if changes were made. The images or other third party material in this article are included in the article’s Creative Commons licence, unless indicated otherwise in a credit line to the material. If material is not included in the article’s Creative Commons licence and your intended use is not permitted by statutory regulation or exceeds the permitted use, you will need to obtain permission directly from the copyright holder. To view a copy of this licence, visit <http://creativecommons.org/licenses/by/4.0/>.

**References**

Acha EM, Mianzan HW, Guerrero RA et al (2004) Marine fronts at the continental shelves of austral south america: Physical and ecological processes. *J Mar Syst* 44(1):83–105. <https://doi.org/10.1016/j.jmarsys.2003.09.005>

Ballarotta M, Ubelmann C, Pujol MI et al (2019) On the resolutions of ocean altimetry maps. *Ocean Sci* 15(4):1091–1109. <https://doi.org/10.5194/os-15-1091-2019>

Beauchamp M, Febvre Q, Georgenthum H et al (2023) 4dvarnet-ssh: end-to-end learning of variational interpolation schemes for nadir and wide-swath satellite altimetry. *Geosci Model Dev* 16(8):2119–2147. <https://doi.org/10.5194/gmd-16-2119-2023>

Berden G, Piola AR, Palma ED (2022) Cross-shelf exchange in the southwestern atlantic shelf: Climatology and extreme events. *Front Mar Sci* 249. <https://doi.org/10.3389/fmars.2022.855183>

Bodnariuk N, Simionato CG, Saraceno M (2021) Sam-driven variability of the southwestern atlantic shelf sea circulation. *Cont Shelf Res* 212:104313. <https://doi.org/10.1016/j.csr.2020.104313>

Combes V, Matano RP (2018) The patagonian shelf circulation: Drivers and variability. *Prog Oceanogr* 167:24–43. <https://doi.org/10.1016/j.pcean.2018.07.003>



- Combes V, Matano RP (2019) On the origins of the low-frequency sea surface height variability of the patagonia shelf region. *Ocean Model* 142:101454. <https://doi.org/10.1016/j.ocemod.2019.101454>
- Dong S, Sprintall J, Gille ST (2006) Location of the antarctic polar front from amsr-e satellite sea surface temperature measurements. *J Phys Oceanogr* 36(11). <https://doi.org/10.1175/JPO2973.1>
- Eriksson E (1970) Cross-spectrum analysis of groundwater levels in an esker. *Hydrol Res* 1(4):245–259. <https://doi.org/10.2166/nh.1970.0017>
- Ferrari R, Artana C, Saraceno M et al (2017) Satellite altimetry and current-meter velocities in the malvinas current at 41 s: Comparisons and modes of variations. *J Geophys Res Oceans* 122(12):9572–9590. <https://doi.org/10.1002/2017JC013340>
- Gordon AL (1989) Brazil-malvinas confluence-1984. *Deep Sea Research Part A Oceanog Res Paper* 36(3):359–384
- Guihou K, Piola AR, Palma ED et al (2020) Dynamical connections between large marine ecosystems of austral south america based on numerical simulations. *Ocean Sci* 16(2):271–290. <https://doi.org/10.5194/os-16-271-2020>
- Haigh ID, Marcos M, Talke SA et al (2023) Gesla version 3: A major update to the global higher-frequency sea-level dataset. *Geosci Data J* 10(3):293–314. <https://doi.org/10.1002/gdj3.174>
- Hendricks JR, Leben RR, Born GH et al (1996) Empirical orthogonal function analysis of global topex/poseidon altimeter data and implications for detection of global sea level rise. *J Geophys Res Ocean* 101(C6):14131–14145. <https://doi.org/10.1029/96JC00922>
- International Altimetry Team (2021) Altimetry for the future: Building on 25 years of progress. *Adv Space Res* 68(2):319–363. <https://doi.org/10.1016/j.asr.2021.01.022> 25 Years of Progress in Radar Altimetry
- Kahl LC, Bianchi AA, Osiroff AP et al (2017) Distribution of sea-air co2 fluxes in the patagonian sea: Seasonal, biological and thermal effects. *Cont Shelf Res* 143:18–28. <https://doi.org/10.1016/j.csr.2017.05.011>
- Lago LS, Saraceno M, Martos P et al (2019) On the wind contribution to the variability of ocean currents over wide continental shelves: A case study on the northern argentine continental shelf. *J Geophys Res Ocean* 124(11):7457–7472. <https://doi.org/10.1029/2019JC015105>
- Lago LS, Saraceno M, Piola AR et al (2021) Volume transport variability on the northern argentine continental shelf from in situ and satellite altimetry data. *J Geophys Res Ocean* 126(2):e2020JC016813. <https://doi.org/10.1029/2020JC016813>
- Lyon DA (2009) The discrete fourier transform, part 4: spectral leakage. *J Object Technol* 8(7). <https://doi.org/10.5381/jot.2009.8.7.c2>
- Matano RP, Palma ED (2018) Seasonal variability of the oceanic circulation in the gulf of san jorge, argentina. *Oceanography* 31(4):16–24
- Matano RP, Palma ED, Piola AR (2010) The influence of the brazil and malvinas currents on the southwestern atlantic shelf circulation. *Ocean Sci* 6(4):983–995. <https://doi.org/10.5194/os-6-983-2010>
- Meccia V, Simionato C, Fiore M et al (2009) Sea surface height variability in the rio de la plata estuary from synoptic to inter-annual scales: Results of numerical simulations. *Estuar Coast Shelf Sci* 85(2):327–343. <https://doi.org/10.1016/j.ecss.2009.08.024>
- Palma ED, Matano RP, Piola AR et al (2004) A comparison of the circulation patterns over the southwestern atlantic shelf driven by different wind stress climatologies. *Geophys Res Lett* 31(24). <https://doi.org/10.1029/2004GL021068>
- Passaro M, Juhl MC (2023) On the potential of mapping sea level anomalies from satellite altimetry with random forest regression. *Ocean Dyn* 73(2):107–116. <https://doi.org/10.1007/s10236-023-01540-4>
- Piola AR, Matano RP, Palma ED et al (2005) The influence of the plata river discharge on the western south atlantic shelf. *Geophys Res Lett* 32(1)
- Piola A, Matano R, Steele J et al (2001) Brazil and falklands (malvinas) currents. *Ocean Curr* 35–43
- Raichich F (2008) A review of sea level observations and low frequency sea-level variability in south atlantic. *Phys Chem Earth (Pt A B C)* 33(3–4):239–249. <https://doi.org/10.1016/j.pce.2007.04.001>
- Ramírez F, Afán I, Davis LS et al (2017) Climate impacts on global hot spots of marine biodiversity. *Sci Adv* 3(2):e1601198. <https://doi.org/10.1126/sciadv.1601198>
- Ruiz Etcheverry LA, Saraceno M, Piola AR et al (2016) Sea level anomaly on the patagonian continental shelf: Trends, annual patterns and geostrophic flows. *J Geophys Res Ocean* 121(4):2733–2754. <https://doi.org/10.1016/j.csr.2014.10.006>
- Ryan HF, Noble MA (2006) Alongshore wind forcing of coastal sea level as a function of frequency. *J Phys Oceanogr* 36(11):2173–2184. <https://doi.org/10.1175/JPO2972.1>
- Saraceno M, Simionato CG, Ruiz-Etcheverry LA (2014) Sea surface height trend and variability at seasonal and interannual time scales in the Southeastern South American continental shelf between 27°S and 40°S. *Cont Shelf Res* 91:82–94. <https://doi.org/10.1016/j.csr.2014.09.002>
- Saraceno M, Bodnariuk N, Ruiz-Etcheverry L et al (2024) Lagrangian characterization of the southwestern atlantic from a dense surface drifter deployment. *Deep-Sea Res I Oceanogr Res Pap* 208:104319. <https://doi.org/10.1016/j.dsr.2024.104319>
- Saraceno M, Provost C, Piola AR et al (2004) Brazil malvinas frontal system as seen from 9 years of advanced very high resolution radiometer data. *J Geophys Res Ocean* 109(C5). <https://doi.org/10.1029/2003JC002127>
- Simionato CG, Meccia VL, Dragani WC et al (2006) Río de la plata estuary response to wind variability in synoptic to intraseasonal scales: Barotropic response. *J Geophys Res Ocean* 111(C9). <https://doi.org/10.1029/2005JC003297>
- Simionato CG, Vera CS, Siegmund F (2005) Surface wind variability on seasonal and interannual scales over rio de la plata area. *J Coastal Res* 21(4):770–783. <https://doi.org/10.2112/008-NIS.1>
- Simpson JH, Sharples J (2012) Introduction to the Physical and Biological Oceanography of Shelf Seas. Cambridge University Press. <https://doi.org/10.1017/CBO9781139034098>
- Stammer D, Wunsch C, Ponte RM (2000) De-aliasing of global high frequency barotropic motions in altimeter observations. *Geophys Res Lett* 27(8):1175–1178. <https://doi.org/10.1029/1999GL011263>
- Stramska M (2013) Temporal variability of the baltic sea level based on satellite observations. *Estuar Coast Shelf Sci* 133:244–250. <https://doi.org/10.1016/j.ecss.2013.09.002>
- Strub PT, James C, Combes V et al (2015) Altimeter-derived seasonal circulation on the southwest atlantic shelf: 27°–43° s. *J Geophys Res Ocean* 120(5):3391–3418. <https://doi.org/10.1002/2015JC010769>
- Thomson RE, Emery WJ (2014) Data analysis methods in physical oceanography. Newnes
- Volkov DL, Larnicol G, Dorandeu J (2007) Improving the quality of satellite altimetry data over continental shelves. *J Geophys Res Ocean* 112(C6). <https://doi.org/10.1029/2006JC003765>
- Woodworth PL, Melet A, Marcos M et al (2019) Forcing factors affecting sea level changes at the coast. *Surv Geophys* 40(6):1351–1397. <https://doi.org/10.1007/s10712-019-09531-1>